J Mater Sci: Mater Electron (2015) 26:5937–5945
DOI 10.1007/s10854-015-3165-2

Facile fabrication of ZnO nanocrystalline-modified graphene hybrid nanocomposite toward methane gas sensing application

Dongzhi Zhang[1,2] · **Nailiang Yin**[1] · **Bokai Xia**[1]

Received: 10 March 2015 / Accepted: 4 May 2015 / Published online: 13 May 2015

Abstract In this paper, we synthetized a hybrid composite of zinc oxide (ZnO) nanocrystalline-decorated reduced graphene oxide (rGO) via a facile hydrothermal process, and fabricated a methane gas sensor by using the ZnO–rGO hybrid composite as sensing film coated on a ceramic tube with Ni–Cr heater. The presence of nanorod-shaped ZnO nanocrystalline and rGO nanosheets was characterized by scanning electron microscopy, X-ray diffraction, transmission electron microscopy and X-ray photoelectron spectroscopy, UV–Vis diffuse reflectance and photoluminescence spectra measurement. The sensing properties of the ZnO–rGO film sensor were investigated by exposing to various concentration of methane gas at different temperature. It was found that the presented sensor exhibited unique advantages in methane gas sensing with concentration spanning from 100 to 4000 ppm, such as outstanding repeatability, fast response-recovery time as well as good selectivity, at an optimal operating temperature of 190 °C. The gas response of the ZnO–rGO hybrid composite was superior to that of the pure ZnO and rGO counterpart in methane gas sensing. The possible and proposed sensing mechanism for the sensor is mainly attributed to its nano-hybrid structure and special interactions at p–n heterojunction. This observed results highlight the ZnO–rGO hybrid composite as a candidate material for constructing methane gas sensors.

✉ Dongzhi Zhang
dzzhang@upc.edu.cn

[1] College of Information and Control Engineering, China University of Petroleum (East China), Qingdao 266580, People's Republic of China

[2] National Engineering Laboratory for Ultra High Voltage Engineering Technology (Kunming, Guangzhou), Guangzhou 510080, People's Republic of China

1 Introduction

Methane is a kind of colorless but dangerous and flammable gases in nature. The measurement of methane gas is increasingly essential for domestic and industrial applications, such as coal mines, petroleum industries, natural sources and indoor environment [1–4]. Especially, methane gas can react with other pollutants in the air to produce dangerous explosives. The explosion limit of methane is ~5 %. Therefore, portable, reliable, low-cost and trace level detection of methane gas is greatly required. Gas chromatography has been widely used for decades in laboratory can achieve off-line monitoring but it cannot work on-line [5, 6]. Currently, on-line monitoring techniques including photoacoustic spectrometry [7], infrared spectrometry [8], thermoelectric [9, 10], optical fibre [11, 12] and quartz crystal microbalance (QCM) [13, 14], have been devoted for detecting methane gas. However, these methods take time and require large instruments that are costly and not portable.

Various metal-oxide semiconductors (MOS), such as PdO [15], SnO_2 [16], Ni_2O_3 [17], ZnO [18], are widely used as gas sensors. Mehrabadi [19] prepared Cu doped cobalt oxide nanocrystals by sol–gel technique, while its methane gas-sensing measurement revealed that the optimal operating temperature is 300 °C. Wagner et al. [20] reported a Pd-doped SnO_2 film methane sensor working at oxidation state of Pd species under high temperature of 600 °C. Among MOS groups, Zinc oxide (ZnO), with band gap energy of 3.37 eV, is one of the most promising material in gas sensing applications due to its high conductive

electron mobility and good adsorption characteristics [21–25]. However, drawbacks like low sensitivity, poor selectivity and high working temperature are still great challenges associated with these sensors [26]. In order to overcome the shortcomings and to enhance sensing characteristics, the modification of ZnO by other atoms has attracted considerable interest [27–29]. Noteablely, graphene or reduced graphene oxide (rGO) is an amazing wonder material with unique electrical chemical and thermal properties that have never been observed in conventional materials [30–32]. Particularly, the extremely high carrier mobility of graphene nanosheets at room temperature indicates that graphene is a promising candidate for gas detection at room temperature. Therefore, the doping of ZnO by graphene may be an alternative route to construct high-performance gas sensors due to graphene can play a vital role in enhancing the free electrons transfer and sensing properties [33].

In this paper, we synthetized a hybrid composite of ZnO–rGO via a facile hydrothermal route, and fabricated a methane gas sensor by using the ZnO–rGO hybrid composite as sensing material coated on a ceramic tube with Ni–Cr heater. The microstructure of ZnO–rGO sample was characterized by using SEM, XRD, TEM and XPS, DRS and PL measurement. The gas sensing properties of the ZnO–rGO film sensor, such as optimal operating temperature, repeatability, selectivity and response-recovery characteristic, were investigated upon exposure of various concentration of methane gas. Finally, the possible sensing mechanism for the sensor was discussed in detail.

2 Experiment

2.1 Materials

Graphite powder (99.8 %), sodium nitrate ($NaNO_3$), sodium hydroxide (NaOH), sulfuric acid (H_2SO_4) and potassium permanganate ($KMnO_4$) were supplied by Aladdin Industrial Corp. (Shanghai, China). Zinc nitrate hexahydrate $Zn(NO_3)_2{\cdot}6H_2O$ was purchased from Sinopharm Chemical Reagent Co. Ltd. All reagents were analytical grade and used as received without further purification.

2.2 Fabrication

Graphene oxide (GO) was synthetized by oxidizing graphite powder based on a modified Hummers' method. In a typical procedure, 60 mL of concentrated H_2SO_4 was added to a mixture of 1 g of graphite powder and 0.8 g of $NaNO_3$ under gentle stirring in an ice bath for overnight. After this, 3.0 g of $KMnO_4$ was added gradually into the solution with the temperature of 20 °C. The mixture was continuously stirred for another 24 h. Subsequently, the resulting solution was added to 250 mL of deionized (DI) water and heated at 90 °C until it turned golden yellow. At last, the obtained solution was filtered and washed with DI water for several times to remove metal ions and the acid. The as-obtained graphene oxide was re-dispersed in water by ultrasonication for 2 h and then frozen-dried to store for further use.

The sensing film of ZnO–rGO hybrid was prepared by using a facile and low-cost method of hydrothermal treatment of $Zn(NO_3)_2$ solution in the presence of rGO. Figure 1 shows the preparation of ZnO–rGO hybrid via hydrothermal treatment. In the typical process, 416 mg of $Zn(NO_3)_2{\cdot}6H_2O$ was firstly dissolved into 30 mL of DI water with stirring for 1 h. Then, 2 mL of GO suspension (0.5 mg/mL) and 4 mL of NaOH solution (160 mg/mL) were added into the resulting solution with stirring for 30 min. Followed by transferring the obtained solution into a 50 mL Teflon-lined, stainless-steel autoclave and then heated for 12 h at 180 °C. GO was converted into conductive rGO under hydrothermal reduction. Afterward, when the autoclave cooled down to room temperature, the final product of ZnO–rGO suspension was washed with DI water for several times to remove excess chloride ions, and subsequent was ultrasonicated for 1 h and centrifugated at 2000 r/min for 15 min.

The gas sensor was fabricated through coating a ceramic tube with the ZnO–rGO dispersion to form a thin film, and

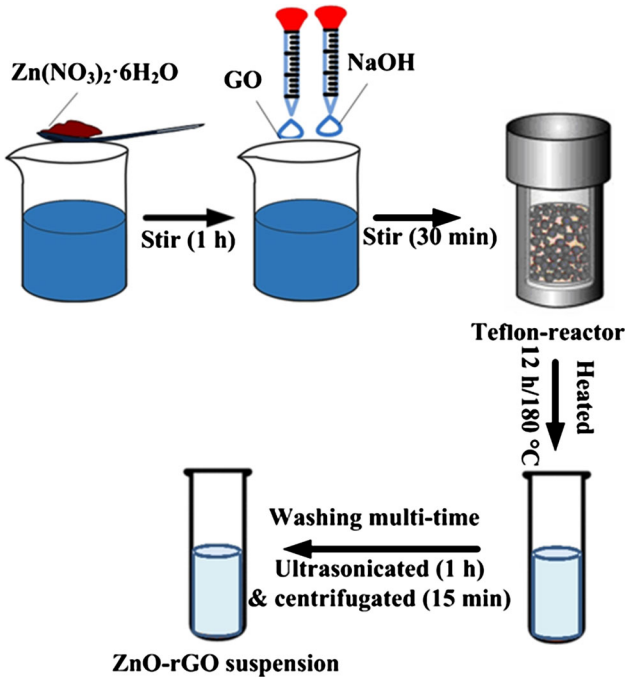

Fig. 1 Preparation of ZnO–rGO suspension via hydrothermal treatment

then was dried in air at 80 °C for 6 h. The structure of the as-fabricated sensor and a theoretical diagram of the test circuit are shown in Fig. 2. The sensor outline dimension is inner diameter 0.6 mm × length 4 mm. A pair of gold electrodes installed at each end of the ceramic tube was used as signal electrodes. A Ni–Cr heating coil threaded the ceramic tube was used as a heating resistor.

2.3 Instrument and analysis

The surface microscopes of ZnO, rGO, ZnO–rGO nanocomposite were measured with field emission scanning electron microscopy (FESEM, Hitachi S-4800). The XRD spectrum for GO, rGO, ZnO nanocrystalline and ZnO–rGO hybrid composite were characterized with X-ray diffractometer (Rigaku D/Max 2500PC, Japan). Transmission electron microscopy (TEM) measurement was performed on a FEI Tecnai G2 F20 electron microscopy with an accelerating voltage of 200 kV. X-ray photoelectron spectroscopy (XPS) analysis was measured on a Thermo Scientific K-Alpha XPS spectrometer to confirm the atomic composition of elements in the ZnO–rGO sample. The optical properties of the samples were characterized by a UV-2600 ultraviolet/visible diffuse reflectance spectrophotometer (DRS). The photoluminescence spectra (PL) were measured with a Hitachi F-2500 fluorescence spectrophotometer.

A schematic diagram of the experimental setup for exposure of methane gas is shown in Fig. 2. The methane gas sensing properties were investigated by exposing the ZnO–rGO film sensor to various concentrations of methane gas, which was achieved by injecting a desired quantity of methane gas into a sealed chamber by using a syringe. The electrical resistance of presented film sensor was measured in DC mode using a data logging/switch unit (Agilent 34970A), which was connected to a PC through RS-232 interface. The operating temperature was controlled by applying a voltage to the heating coil through a power source (Gwinstek GPD-4303S). The response of the gas sensor as a function of methane gas was achieved by exposing the gas sensor to different concentrations of methane gas. The figure of merit used for the evaluation of sensor performance was the sensitivity (S), determined by $S = \Delta R/R_a = (R_a - R_g)/R_a \times 100\ \%$, where R_a and R_g were the electrical resistance of the sensor in the given methane concentration and air without methane, respectively.

3 Results and discussion

3.1 Sample characterization

The SEM and XRD characterization results are shown in Fig. 3. Figure 3a shows the as-prepared ZnO was nanorod-shaped crystal. Figure 3b indicates that the rGO has wrinkles which overlap at the edges, and also exhibits randomly aggregated rGO sheets. Figure 3c shows the ZnO–rGO film is constructed by ZnO nanorods and rGO

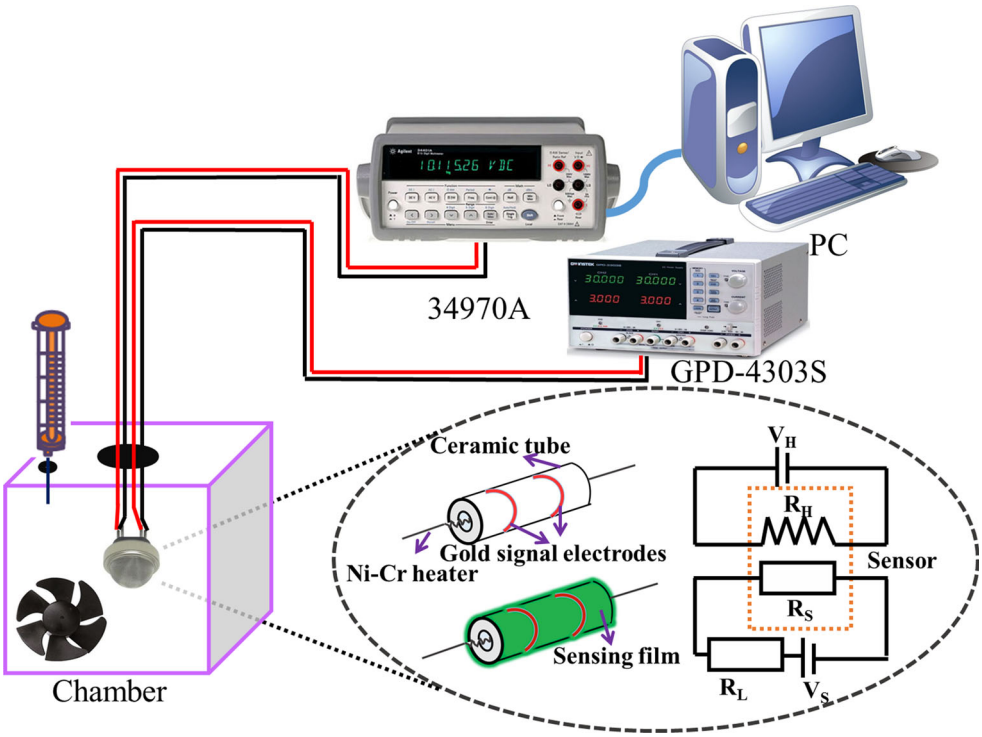

Fig. 2 Schematic of experimental setup used for methane gas sensing

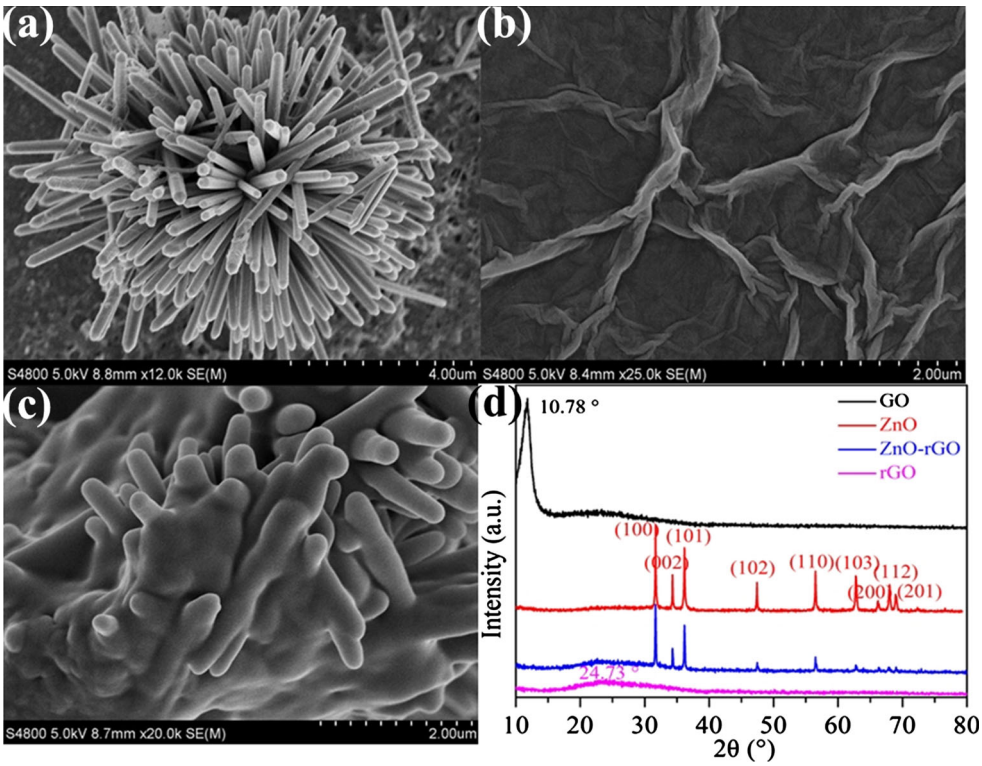

Fig. 3 SEM characterization of **a** ZnO, **b** rGO, **c** ZnO–rGO sample, and **d** XRD spectrum for GO, rGO, ZnO and ZnO–rGO samples

sheets wrapped closely together. The XRD measurement is performed by using Cu Kα ($\lambda = 1.5418$ Å) radiation with a 2θ scanning range of 10–80°. Figure 3d plots the XRD spectrum for GO, rGO, ZnO nanocrystalline and ZnO–rGO hybrid composite film. A peak at 2θ angle of 10.78° for GO and a peak at 2θ angle of 24.73° for rGO were obviously observed. The interlayer distances of 8.27 Å ($2\theta = 10.78°$) for GO and 3.60 Å ($2\theta = 24.73°$) for rGO were determined according to the well-known Bragg formula. The rGO was shrunk from the initial GO due to many oxygen-containing groups on GO sheets were dislodged through thermal reduction, and further confirmed the successful preparation of rGO through hydrothermal treatment. XRD of the ZnO showed polycrystalline structure with major peaks in the planes (1 0 0), (0 0 2) and (1 0 1). It is observed that the peak related to rGO is not obvious in the XRD spectrum of ZnO–rGO at 2θ around 24.73°, probably due to the weak peak of rGO is swamped by the presence of the strong peak of the ZnO nanocrystalline.

The as-prepared ZnO–rGO sample was further investigated by using TEM and XPS measurement. The TEM image of ZnO–rGO sample shown in Fig. 4a exhibits ZnO nanorods are distributed on the surface of rGO sheets. The size of ZnO nanorods is observed with 1 μm in diameter and 5 μm in length. The absence of ZnO nanorods reveals that hydrothermal treatment of GO and Zinc nitrate solution is an effective method for the preparation of ZnO–rGO nanocomposites. Figure 4b shows the highly resolution TEM (HRTEM) image of the ZnO polycrystallines. The measured spacing between adjacent lattice fringes are 0.31 nm, corresponding to the (1 0 0) plane of the ZnO polycrystalline. Figure 4c shows the XPS spectrum of ZnO–rGO sample. The XPS result exhibits that several peaks at 11, 90, 140, 285, 531, 1022 and 1046 eV associated with Zn3d, Zn3p, Zn3s, C1s, O1s, Zn2p3 and Zn2p1 bands, respectively, indicating the presence of Zn, C and O elements in the samples. Figure 4d shows the C1s spectrum of ZnO–rGO sample. It is visible that the sample exhibits three peaks at 284.58, 288.78 and 285.58 eV, associated with C–C, C=O and C–O, respectively. Compared with the peak intensity of C=O and C–O in GO reported in Refs. [34, 35], the peak intensity of C=O and C–O in ZnO–rGO sample is much lower and the C–C bond becomes dominant, suggesting the majority oxygen-containing groups are successfully removed after hydrothermal treatment.

The UV–Vis diffuse reflectance spectra (DRS) were measured to characterize the optical properties of ZnO and ZnO–rGO samples. The DRS results are shown in Fig. 4e. It is visible that pure ZnO absorb ultraviolet light while the ZnO–rGO sample exhibits an enhanced absorption over pure ZnO in the visible light region. This phenomenon was also observed from TiO_2–rGO nanocomposite reported in Ref. [36]. The change of electron transfer between ZnO and rGO was investigated by photoluminescence (PL) measurements. Figure 4f shows the PL spectra of ZnO and ZnO–rGO samples. Pure ZnO displays a broad PL emission

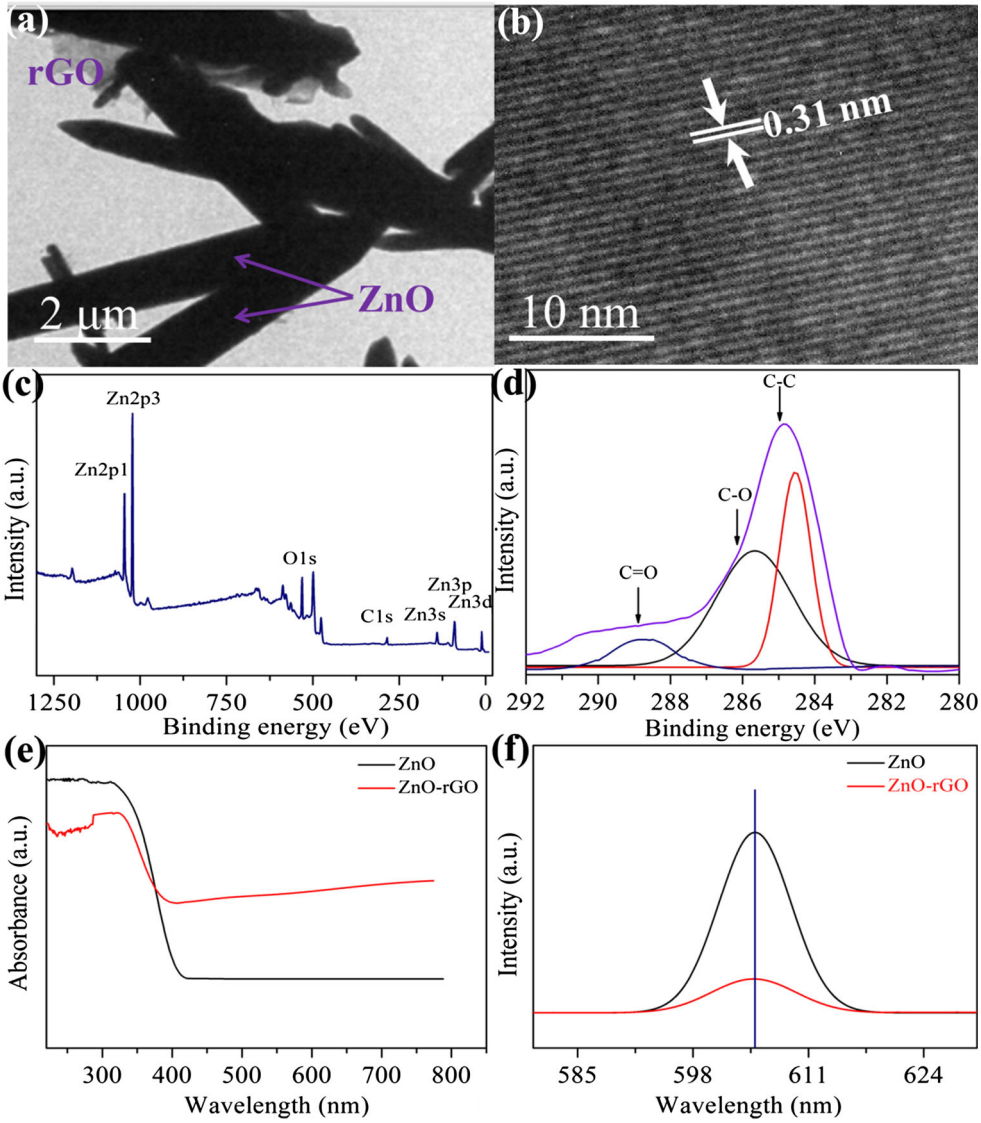

Fig. 4 **a** TEM image of ZnO–rGO sample, **b** high resolution TEM image of ZnO polycrystalline, **c** XPS spectrum of ZnO–rGO sample, **d** C1s spectrum of ZnO–rGO sample, **e** DRS of ZnO and ZnO–rGO samples, **f** PL spectra of ZnO and ZnO–rGO samples

peak at 604 nm, while ZnO–rGO exhibits a major decrease in the PL intensity compared to pure ZnO. The weaker intensity of the peak represents the lower recombination probability of free charges, indicating that coupling with rGO can effectively mitigate the recombination of photo-generated electron–hole pairs of ZnO [37].

3.2 Methane gas sensing properties

The optimal operating temperature of ZnO–rGO film sensor for determining methane gas was investigated by performing the gas sensing experiments at different temperatures. Figure 5 shows the sensitivity and resistance responses of the ZnO–rGO film sensor upon exposure of 1000 ppm methane gas at operating temperature ranging from 100 to 260 °C. The sensor sensitivity was increased rapidly and reached a maximum value at 190 °C, and then

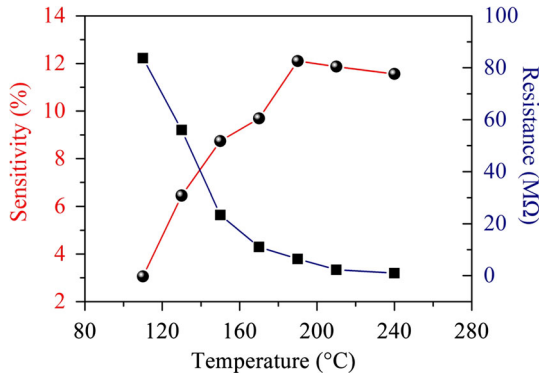

Fig. 5 The sensitivity and resistance response of ZnO–rGO film sensor to 1000 ppm methane gas at different operating temperature

decreased with further increasing of the operating temperature. The maximum sensitivity of the ZnO–rGO film sensor to 1000 ppm methane gas is about 12.1 % at the

operating temperature of 190 °C. Therefore, we choose 190 °C as the operating temperature to perform the subsequent investigation for methane gas sensing. The resistance–temperature behavior shown in Fig. 5 indicates the resistance values of the ZnO–rGO film sensor decreases with increasing operating temperature from 100 to 260 °C due to the intrinsic characteristics of the semiconductor. The resistance value of as-prepared ZnO–rGO film sensor was about 6 MΩ at the temperature of 190 °C.

Figure 6 demonstrates the typical time-dependent response and recovery curves of the ZnO–rGO film sensor. Several methane pulses for the sensor from air to various concentrations were investigated. The time taken by the sensor to achieve 90 % of the total resistance change was defined as the response or recovery time. Response time and recovery time of less than 30 and 40 s were observed, respectively.

Figure 7 shows the repeatability of ZnO–rGO film sensor performed for three different concentrations of methane gas at operating temperature of 190 °C. The repeatability characteristics were measured for four exposure/recovery cycles under 500, 1500 and 4000 ppm methane gas, respectively. The exposure and recovery time for the sensor is ~200 s. It is visible that the ZnO–rGO film sensor exhibited a clear response-recovery behavior and acceptable repeatability towards methane gas.

Figure 8 plots the sensor sensitivity as a function of methane gas concentration for ZnO–rGO, ZnO and rGO film at 190 °C. The sensitivities of these sensors were investigated toward methane gas in a wide range of 100–4000 ppm. The gas response of the ZnO–rGO hybrid composite was superior to that of the pure ZnO and rGO counterpart in methane gas sensing. It is visible that the pure rGO film is basically no response upon exposure of methane gas. The ZnO–rGO film sensor exhibits a higher

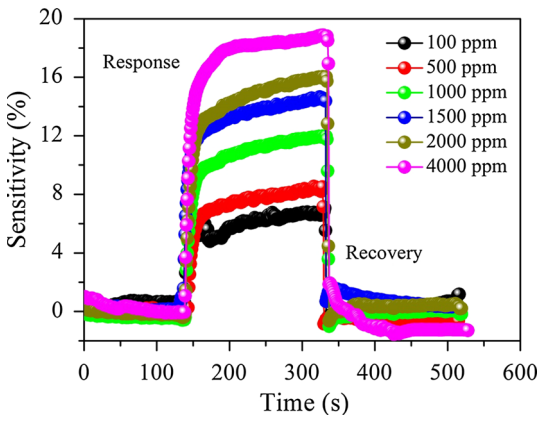

Fig. 6 Typical response and recovery *curves* of the ZnO–rGO film sensor upon exposure of methane gas with various concentrations at 190 °C

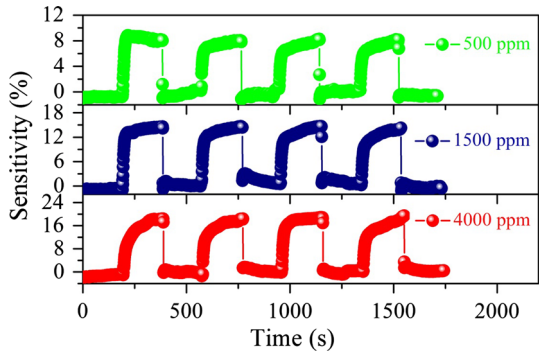

Fig. 7 Repeatability of ZnO–rGO film sensor exposed to 500, 1500 and 4000 ppm of methane gas at 190 °C

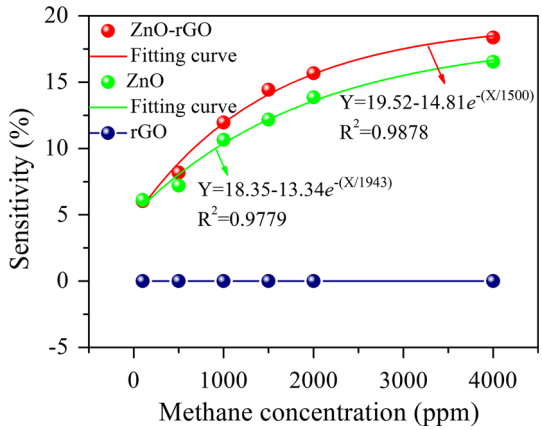

Fig. 8 The sensor sensitivity as a function of methane gas concentration for ZnO–rGO, ZnO and rGO film at 190 °C

sensitivity than that of pure ZnO sensor, and the fitting equation for the sensor sensitivity Y and gas concentration (ppm) X can be depicted as $Y = 19.52 - 14.81e^{-(X/1500)}$ and $Y = 18.35 - 13.34e^{-(X/1943)}$ for ZnO–rGO and pure ZnO film sensor, respectively, and the linear regression coefficient, R^2, is 0.9878 and 0.9779, respectively.

Figure 9 shows the real-time resistance measurement of the ZnO–rGO film sensor exposed to cumulative concentrations of methane at 190 °C. The cumulative concentrations of methane were performed in a wide range from 0 (dry air) to 4000 ppm, and the exposure time under each concentration was selected 200 s. The resistance response decreased with the cumulative concentration of methane gas. The abrupt resistance change for the sensor switching from one concentration to another indicating a fast response time.

As well known, selectivity to target gas is always one of the key factors to gas sensors. The selectivity of ZnO–rGO film was investigated by exposing it to 1000 ppm of various gas species at 190 °C, including $C_6H_5CH_2OH$, H_2, NH_3, CH_4, CO_2, C_3H_8O, CH_3COOH, and the measured result is shown in Fig. 10. Under the same conditions, the

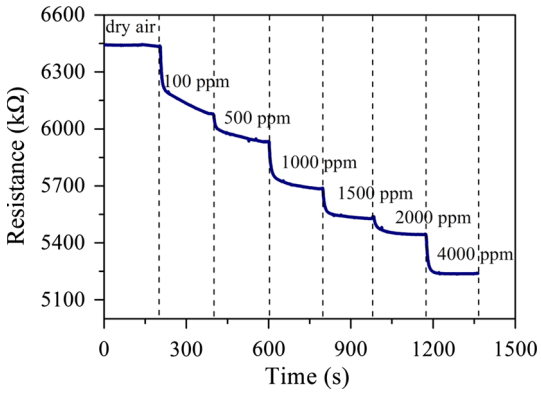

Fig. 9 Resistance measurement of the ZnO–rGO film sensor under switching concentration of methane gas at 190 °C

ZnO–rGO film sensor exhibits much higher sensitivity to methane gas than those of other tested vapors, indicating a high selectivity toward methane detection. Table 1 presents the performance of the proposed methane gas sensor in comparison with previous works [38–42]. The response, measuring concentration and operating temperature for the prepared sensor are comparable to those of the sensor made from metal oxide counterparts by using sol–gel, colloid mixing, MEMS, and layer-by-layer self-assembly techniques. The one-step facile hydrothermal prepared ZnO–rGO sample exhibited higher sensitivity at relative low temperature.

3.3 Methane-sensing mechanism

The above sensing experimental results demonstrated that ZnO–rGO film is very sensitive to methane gas absorption, highlighting the ZnO–rGO hybrid composite is an excellent candidate material for constructing methane gas sensors. The enhanced sensing performance of the ZnO–rGO hybrid composite possibly attributed to three factors.

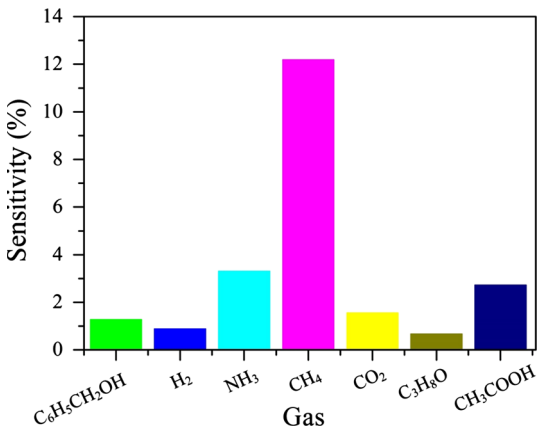

Fig. 10 The selectivity of the ZnO–rGO film sensor towards 100 ppm of various gases at 190 °C

Firstly, the incorporation of rGO nanosheets has a significant effect on preventing the aggregation of ZnO polycrystals, leading to a formation of hybrid nanostructure with much higher surface area and more active sites, which greatly facilitates the adsorption and diffusion of methane gas molecules. Furthermore, rGO has amazing electrical properties such as high carrier mobility and low 1/*f* noise, which can result in electrons quickly transfer to the surface of the sensing film. Thus, the decoration of rGO in the ZnO–rGO hybrid provided a highly conductive carbon film serving as an anchor for the ZnO nanoparticles.

Secondly, the gas-sensing mechanism associated to the adsorbed oxygen species on the ZnO surface is supposed to be another contribution. Chemisorbed oxygen molecules in the atmosphere are ionized to oxygen ions through capturing free electrons from the surface of ZnO. As reported in Refs. [18, 26], one adsorbed oxygen molecule attracts one electron from the conduction band of ZnO to form O_2^-, which takes place at room temperature and O_2^- persists up to 150 °C. As the operating temperature of the sample is above 150 °C, the as-formed O_2^- further takes up another electron from the conduction band of ZnO, resulting in the formation of O^-. The reaction mechanism can be briefed as:

$$O_2(\text{gas}) \rightarrow O_2(\text{ads}) \quad (1)$$

$$O_2(\text{ads}) + e^- \rightarrow O_2^-(\text{ads}) \quad (2)$$

$$O_2^-(\text{ads}) + e^- \rightarrow 2O^-(\text{ads}) \quad (3)$$

The mechanism for oxygen absorption and methane gas sensing on the ZnO–rGO film is shown in Fig. 11a. Such reactions lead to the sensor in a high resistance state in air. When the sensor is exposed to the methane gas, the gas molecules react with the oxygen ions on the surfaces of sensing film, and the reactions are as follows [43–45]:

$$O_2^-(\text{ads}) + CH_4 \rightarrow CO_2 + H_2O + 2e^- \quad (4)$$

$$O^-(\text{ads}) + CH_4 \rightarrow CO_2 + H_2O + e^- \quad (5)$$

Such reactions leads to a decrease of oxygen ions concentration and retrieve the trapped electrons back to the conduction band of the ZnO, resulting in a decrease in the sensor resistance when exposed to the target gases [46].

Thirdly, the contribution of the heterojunction at the interface of rGO and ZnO probably plays a crucial role toward gas sensing [47, 48]. P–n heterojunctions can be created at the interface between n-type ZnO and p-type rGO sheets. The space charge region (the depletion layer) is created by the oxygen ions on the ZnO surface. The schematic energy diagram of the heterojunction between ZnO and rGO is shown in Fig. 11b. The differences in the bandgap and Fermi level between the rGO and the ZnO are modified through band bending in the depletion layer when adsorbing or desorbing methane molecules. The adsorbed

Table 1 Performance of the presented sensor in this work compared with previous work

Sensor type	Sensing material	Technique used	Concentration (ppm)	Response (/kppm)	Temp. (°C)	References
Resistive	ZnO–rGO	Hydrothermal	100–4000	4.52 %	190	This paper
Resistive	Cu doped cobalt oxide	Sol–gel	3000–6000	4 %	300	[36]
Voltage	Pd/θ–Al_2O_3	Colloid mixing	1–1000	0.5 mV	400	[37]
Voltage	Noble metal doped SnO_2	MEMS	1158–4630	0.13 mV	324	[38]
Voltage	Pt/α–Al_2O_3	Deposition	200–2000	0.39 mV	391	[39]
QCM	PANI/PdO	LbL self-assembly	3000–8000	5 Hz	RT	[40]

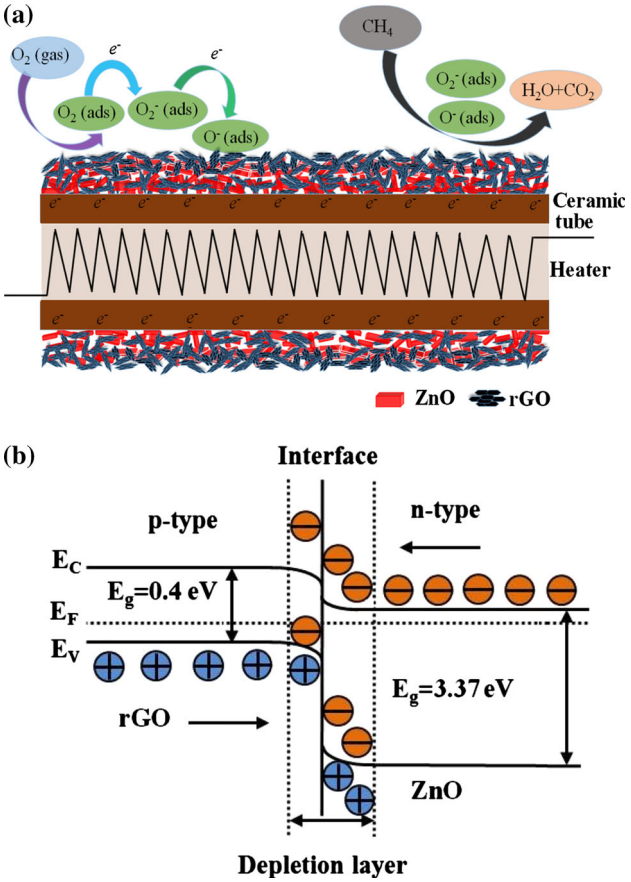

Fig. 11 **a** Mechanism for oxygen absorption and methane gas sensing on the ZnO–rGO film. **b** p–n heterojunction for ZnO–rGO film sensor

gas molecules at the p–n heterojunction lead to a reduction of oxygen ions concentration and a decrease of the depletion layer, and subsequently result in a fall of sensor resistance.

4 Conclusions

In summary, we synthetized a hybrid composite of ZnO–rGO via a facile hydrothermal route, and fabricated a methane gas sensor by using the ZnO–rGO nanocomposite as sensing film coated on a ceramic tube with Ni–Cr heater. SEM, XRD, TEM, XPS, DRS and PL measurement was used to characterize the ZnO–rGO samples. The gas sensing properties of the ZnO–rGO film sensor were investigated upon exposure of various concentration of methane gas. As a result, the sensor exhibited excellent sensing properties such as outstanding repeatability, fast response-recovery time as well as good selectivity at an optimal operating temperature of 190 °C. The possible and proposed sensing mechanism for the sensor is mainly due to its nano-hybrid structure and special interactions at p–n heterojunction. This observed results highlight the ZnO–rGO hybrid as a candidate material for constructing methane gas sensors.

Acknowledgments This work was supported by the National Natural Science Foundation of China (Grant No. 51407200), the Science and Technology Plan Project of Shandong Province (Grant No. 2014GSF117035), the Promotive Research Foundation for the Excellent Middle-Aged and Youth Scientists of Shandong Province of China (Grant No. BS2012DX044), the Science and Technology Development Plan Project of Qingdao (Grant No. 13-1-4-179-jch), the Open Fund of National Engineering Laboratory for Ultra High Voltage Engineering Technology (Kunming, Guangzhou) (Grant No. NEL201518), the Fundamental Research Funds for the Central Universities of China (Grant No. 15CX05041A), and the Science and Technology Project of Huangdao Zone, Qingdao, China (Grant No. 2014-1-51).

Conflict of interest The authors declared that they have no conflicts of interest to this work.

References

1. A.E. Milne, M.J. Glendining, P. Bellamy, T. Bellamy, S. Gilhespy, C. Rivas, A. Hulin, O.M. Van, A.P. Whitmore, Atmos. Environ. **82**, 94 (2014)
2. A.K. Prasad, S. Amirthapandian, S. Dhara, S. Dash, N. Murali, A.K. Tyagi, Sens. Actuators B Chem. **191**, 252 (2014)
3. J. Yu, H. Wen, M. Shafiei, M.R. Field, Z.F. Liu, W. Wlodarski, N. Motta, Y.X. Li, K. Kalantar-Zadeh, P.T. Lai, Sens. Actuators B Chem. **184**, 118 (2013)
4. N.M. Vuong, N.M. Hieu, H.N. Hieu, H. Yi, D. Kim, Y. Han, M. Kim, Sens. Actuators B Chem. **192**, 327 (2014)
5. E. Flores, G.C. Rhoderick, J. Viallon, P. Moussay, T. Choteau, L. Gameson, F.R. Guenther, R.I. Wielgosz, Anal. Chem. **87**, 3272 (2015)

6. Y. Liu, Y. Shang, G. Shan, Ind. Eng. Chem. Res. **53**, 19533 (2014)
7. M.G. González, X. Liu, R. Niessner, C. Haisch, Sens. Actuators B Chem. **150**, 770 (2010)
8. B. Mortazavi, B.J. Wilson, F. Dong, M. Gupta, D. Baer, Environ. Sci. Technol. **47**, 11676 (2013)
9. D. Nagai, M. Nishibori, T. Itoh, T. Kawabe, K. Sato, W. Shin, Sens. Actuators B Chem. **206**, 488 (2015)
10. N.H. Park, T. Akamatsu, T. Itoh, N. Izu, W. Shin, Sensors **14**, 8350 (2014)
11. J.C. Yang, L. Zhou, J. Huang, C.Y. Tao, X.M. Li, W.M. Chen, Sens. Actuators B Chem. **207**, 477 (2015)
12. J. Shemshad, Sens. Actuators B Chem. **186**, 466 (2013)
13. S. Antonaroli, B. Crociani, C.D. Natale, S. Nardis, M. Stefanelli, R. Paolesse, Sens. Actuators B Chem. **208**, 334 (2015)
14. S. Antonaroli, B. Crociani, C.D. Natale, S. Nardis, M. Stefanelli, R. Paolesse, Sens. Actuators B Chem. **208**, 334 (2015)
15. F. Zhang, C. Hakanoglu, J.A. Hinojosa Jr, J.F. Weaver, Surf. Sci. **617**, 249 (2013)
16. M. Bagheri, A.A. Khodadadi, A.R. Mahjoub, Y. Mortazavi, Sens. Actuators B Chem. **188**, 45 (2013)
17. N.M. Vuong, N.M. Hieu, H.N. Hieu, H. Yi, D. Kim, Y.S. Han, M. Kim, Sens. Actuators B Chem. **192**, 327 (2014)
18. S. Ghosh, C. Roychaudhuri, R. Bhattacharya, H. Saha, N. Mukherjee, A.C.S. Appl, Mater. Interfaces **6**, 3879 (2014)
19. Z.S. Mehrabadi, A. Ahmadpour, N. Shahtahmasebi, M.M.B. Mohagheghi, Phys. Scr. **1**, 801 (2011)
20. T. Wagner, M. Bauer, T. Sauerwald, C.D. Kohl, M. Tiemann, Thin Solid Films **520**, 909 (2011)
21. Y. Hou, A.M. Soleimanpour, A.H. Jayatissa, Sens. Actuators B Chem. **177**, 769 (2013)
22. X.W. Li, W. Feng, Y. Xiao, P. Sun, X.L. Hu, K. Shimanoe, G.Y. Lu, N. Yamazoe, RSC Adv. **53**, 28005 (2014)
23. J. Zhang, T. Liu, Y. Zhang, W. Zeng, F. Pan, X. Peng, J. Mater. Sci. Mater. Electron. **26**, 1347 (2015)
24. Y. Zhang, T. Liu, H. Zhang, W. Zeng, F. Pan, X. Peng, J. Mater. Sci. Mater. Electron. **26**, 191 (2015)
25. C. Zhang, J. Wang, M. Olivier, M. Debliquy, Sens. Actuators B Chem. **209**, 69 (2014)
26. A.S.M.I. Uddin, D.T. Phan, G.S. Chung, Sens. Actuators B Chem. **207**, 362 (2015)
27. L. Yu, S. Liu, B. Yang, J. Wei, M. Lei, X. Fan, Mater. Lett. **141**, 79 (2015)
28. B. Wang, Z.Q. Zheng, L.F. Zhu, Y.H. Yang, H.Y. Wu, Sens. Actuators B Chem. **195**, 549 (2014)
29. H. Tian, H. Fan, H. Guo, N. Song, Sens. Actuators B Chem. **195**, 132 (2014)
30. K.S. Novoselov, V.I. Fal′ko, L. Colombo, P.R. Gellert, M.G. Schwab, K. Kim, Nature **490**, 192 (2012)
31. A.V. Kretinin, Y. Cao, J.S. Tu, G.L. Yu, R. Jalil, K.S. Novoselov, S.J. Haigh, A. Gholinia, A. Mishchenko, M. Lozada, T. Georgiou, C.R. Woods, F. Withers, P. Blake, G. Eda, A. Wirsig, C. Hucho, K. Watanabe, T. Taniguchi, A.K. Geim, R.V. Gorbachev, Nano Lett. **14**, 3270 (2014)
32. J. Liu, Z. Liu, C.J. Barrow, W. Yang, Anal. Chim. Acta **859**, 1 (2015)
33. G. Singh, A. Choudhary, D. Haranath, A.G. Joshi, N. Singh, S. Singh, R. Pasricha, Carbon **50**, 385 (2012)
34. S. Pei, J. Zhao, J. Du, W. Ren, H.M. Cheng, Carbon **48**, 4466 (2010)
35. H. Zhang, J. Feng, T. Fei, S. Liu, T. Zhang, Sens. Actuators B Chem. **190**, 472 (2014)
36. L.L. Tan, W.J. Ong, S.P. Chai, A.R. Mohaed, Nanoscale Res. Lett. **8**, 1–9 (2013)
37. H.N. Tien, V.H. Luan, L.T. Hoa, N.T. Khoa, S.H. Hahn, J.S. Chung, E.W. Shin, S.H. Hur, Chem. Eng. J. **229**, 126–133 (2013)
38. Z.S. Mehrabadi, A. Ahmadpour, N. Shahtahmasebi, M.M.B. Mohagheghi, Phys. Scr. **84**, 015801 (2011)
39. D. Nagai, M. Nishibori, T. Itoh, T. Kawabe, K. Sato, W. Shin, Sens. Actuators B Chem. **206**, 488 (2015)
40. W. Jang, I.-H. Kim, Y.-S. Jeong, K.-B. Park, S.-S. Park, M.-Y. Yoon, Y. Roh, J.-S. Park, J. Electroceram. **31**, 280 (2013)
41. N.-H. Park, T. Akamatsu, T. Itoh, N. Izu, W. Shin, Sensors **14**, 8350 (2014)
42. G. Xie, P. Sun, X. Yan, X. Du, Y. Jiang, Sens. Actuators B Chem. **145**, 373 (2010)
43. D. Haridas, V. Gupta, Sens. Actuators B Chem. **166**, 156 (2012)
44. K. Javad, C.F. Dee, B.Y. Majlis, Appl. Surf. Sci. **134**, 7 (2010)
45. F. Li, Y.L. Yuan, J.Y. Luo, Q.H. Qin, J.F. Wu, Z. Li, X.T. Huang, Appl. Surf. Sci. **256**, 6082 (2010)
46. D.Z. Zhang, A.M. Liu, H.Y. Chang, B.K. Xia, RSC Adv. **5**, 3016 (2015)
47. N. Ganganagappa, E. Gunter, V.G. Renato, R.T. Sergio, E.W. Daniel, D. Jairton, J. Mol. Catal. A **378**, 213 (2013)
48. Y. Wang, Y.H. Tang, Y. Li, X.N. Liu, S.L. Luo, C.B. Liu, J. Mater. Sci. Mater. Med. **48**, 6203 (2013)